IEEE Access
Multidisciplinary | Rapid Review | Open Access Journal

Received July 19, 2019, accepted July 30, 2019, date of publication August 5, 2019, date of current version August 19, 2019.

Digital Object Identifier 10.1109/ACCESS.2019.2933387

DM-Free Curvelet Based Denoising for Astronomical Single Pulse Detection

MIN JIANG[1,2], BINGYI CUI[3], YU-FENG YU[1], AND ZHICHENG CAO[4]

[1]Department of Statistics and Institute of Intelligent Finance, Accounting & Taxation, Guangzhou University, Guangzhou 510006, China
[2]Lane Department of Computer Science and Electrical Engineering, West Virginia University, Morgantown, WV 26505, USA
[3]Department of Physics and Astronomy, West Virginia University, Morgantown, WV 26505, USA
[4]Department of Biomedical Engineering, Xidian University, Xi'an 710126, China

Corresponding authors: Yu-Feng Yu (yuyufeng220@163.com) and Zhicheng Cao (zccao@xidian.edu.cn).

This work was supported in part by the Ministry of Education of Humanities and Social Sciences Interdisciplinary/Comprehensive Study of Youth Project under Grant 14YJCZH019, in part by the Natural Science Foundation of Guandong Province under Grant 2016A030313710 and Grant 2015A030313624, and in part by the Science and Technology Program of Guangzhou under Grant 2016A07010170.

ABSTRACT Rotating radio transients (RRATs) are sporadically emitting pulsars which are detected only through single pulse search. Detecting these single pulses in RRATs observation with high detection accuracy is a challenge due to the background noise. It is better to conduct the single pulse detection directly on the raw time-frequency observation than on the de-dispersed data, because de-dispersion process takes very intensive computation. In this paper, we propose to accomplish this idea by treating two-dimensional (2D) time-frequency data as images and develop a curvelet based denoising approach after studying the characteristics of the RRATs pulses and the noise. The denoising approach estimates the range of curvature (orientations) and width (scales) that describe the RRATs pulses and reconstructs cleaner images from the selected orientations and scales. The proposed denoising approach does not require prior knowledge of exact dispersion measures (DM) value. In addition, a framework of detecting the single pulses from the time-frequency data, named HOG-SVM, is also proposed to further evaluate the curvelet based denoising approach. Compared with the other four denoising approaches, the proposed curvelet based method leads to better detection results, with detection accuracy being increased to 98.7% by HOG-SVM.

INDEX TERMS Astronomical single pulse, curvelet based denoising, DM-free, single pulse detection.

I. INTRODUCTION

In the modern era of computer science, it is of great interest to design algorithms and methods that can be utilized in astronomical research. Astronomical data collected by telescopes are crucial for experimental astronomy, which provides the evidence to reveal the physical or environmental properties of celestial bodies. However, these collected data are usually polluted with celestial or terrestrial interference and noise. Thus it is necessary to develop efficient approaches for denoising and analyzing the astronomical data. In this work, we focus on the astronomical data of a specific celestial body: Rotating Radio Transients (RRATs), which is a special kind of pulsar and is detected only through single pulse search. Different from periodically emitting pulsars, RRATs are sporadic pulsars that emit isolated pulses. The profiles of the pulses are typically a few milliseconds in duration, with intervals between detected pulses ranging from minutes to hours [1].

There are mainly two types of approaches to the search of pulsars in the time domain: periodicity searching [2] and single pulse searching [3]. Both approaches conduct searching on de-dispersed time series but try to detect different phenomena. Periodicity searching aims to detect periodic pulses while single-pulse searching works for isolated transients, such as RRATs, fast radio burst (FRB). Generally, the preparatory steps of both searching approaches are the same: first is radio frequency interference (RFI) removal from the raw time-frequency data, then is to apply de-dispersion to the data. Dispersion is the phenomenon in which adjacent frequency channels are shifted in time to compensate for the frequency-dependent delay introduced as the radio wave travels through the interstellar medium (ISM) by an amount proportional to the dispersion measures (DM) [3]. Because

The associate editor coordinating the review of this manuscript and approving it for publication was Sudhakar Radhakrishnan.

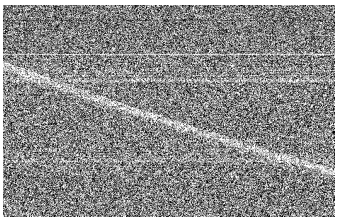

FIGURE 1. A short slice of J1819−1458 time-frequency data which contains a visible curve (a strong pulse). The horizontal lines in the image are caused by interference.

DM is not known as prior knowledge, choosing the optimal trail DM is done by a blind search from thousands of trial DMs. This process takes very intensive computation. Thereby it is desirable to investigate effective denoising and detection approaches for time-frequency data (before de-dispersion) without known of the exact DM value.

In this work, we treat the RRAT time-frequency data as digital images. Fig. 1 shows a short slice of time-frequency data of J1819−1458, which contains a strong (visible) pulse. When the data is viewed in the time-frequency plane, the pulse signal is shown as a visible curve. While most pulses in the wild are too weak to be visible, thereby the main aim of applying denoising to time-frequency data is to make the invisible pulses visible. Such denoising processing is of great benefit to the following single pulse detection. Unfortunately, currently, there are very limited denoising methods specially designed for RRATs time-frequency data. And the conventional denoising methods in image processing area can not meet this special requirement quite well. Because most denoising approaches in the image processing [4]–[6] are designed for portraits or landscapes, which do not contain such strong background noise. Thereby, this work is dedicated to this research area.

Inspired by the curvelet transform theory [7], we propose a curvelet-based denoising method for radio observations of RRATs. The curvature and widths of different RRATs pulses are various because of their distinct intrinsic properties from one another. The curvature is determined by the DM value of the RRATs and is related to the magnetic field of the RRATs. Taking into account the characteristics of the RRAT pulses and the noise, we approximately estimate the range of curvature (orientations) and width (scales) that describes an RRAT pulse (curve) and use these to develop an effective denoising approach. The proposed denoising approach does not require prior knowledge of an exact DM value. Different from most denoising tasks in conventional image processing which use peak signal to noise ratio (PSNR) to evaluate the denoising performance, the final goal of our denoising method is to lead a higher accuracy on single pulse detection. Therefore, to better evaluate the efficiency of the proposed denoising approach, a single pulse detection method from time-frequency data is also developed. Fig. 2 shows the proposed two-stage denoising and detection methods. The input is time-frequency data, which can be considered as grey images. The output is a binary decision for each image. 0 represents no single-pulse detected and 1 represents single-pulse detected from the input image. Comparing with a traditional denoising method, curvelet based method leads to a higher detection accuracy in the single pulse detection stage. And the proposed detection method outperforms another detection method.

The main contributions of this work include:

1) A curvelet-based denoising method is proposed for radio time-frequency data of RRATs which does not require the prior knowledge of the DM value.
2) A framework HOG-SVM is developed for single pulses detection which effectively improves the detection accuracy.
3) Extensive experiments are conducted on a simulated dataset. Based on the experimental results, the proposed curvelet based denoising method outperforms the other four compared methods.

The remainder of the paper begins by providing the related work on denoising methods for astronomical radio observation and general denoising methods in image processing in Section II. Section III gives details about the proposed curvelet-based denoising approach. The single pulse detection framework is presented in Section IV. The simulated dataset, performance matrices, experimental settings, detailed experimental results and analysis are given in Section V. Finally, the conclusions and future works are summarized in Section VI.

II. RELATED WORK

In the past few years, several single pulse searching methods [8], [9], [35] are proposed which include de-dispersion. Cordes and McLaughlin [8] first presented a general methodology for single-pulse search which includes de-dispersion, boxcar filtering, thresholding and determining the real pulses. The one-dimensional boxcar denoising method (also named as the matched filter) was utilized to de-dispersed time series. This conventional denoising method was employed among others by Deneva *et al.* [9], Keane *et al.* [10], Bagchi *et al.* [11] and Cui *et al.* [12] for single-pulse searches. Another RRATs searching algorithms-PRESTO was presented by [9], which utilized a matched filter similar to the method proposed by Cordes and McLaughlin [8], but with a sophisticated RFI excision scheme and a trial DM list. This approach can eliminate the unique RFI generated by radar and the non-periodic RFI detected in multi-beams. However, PRESTO shows less sensitive to weak, narrow pulses but resulted in a significant reduction of RFI events.

Recently, some work studied denoised methods for de-dispersed time-series. Romeo *et al.* [13] designed an efficient wavelet add-on code for removing noisy from cosmological, galaxy and plasma N-body simulations. Eatough *et al.* [14] proposed an RFI removal technique: zero-DM filtering. Since terrestrial RFI does not have the property of dispersion, this method filtered the radio signal with zero DM value. It is effective for suppressing the terrestrial interference.

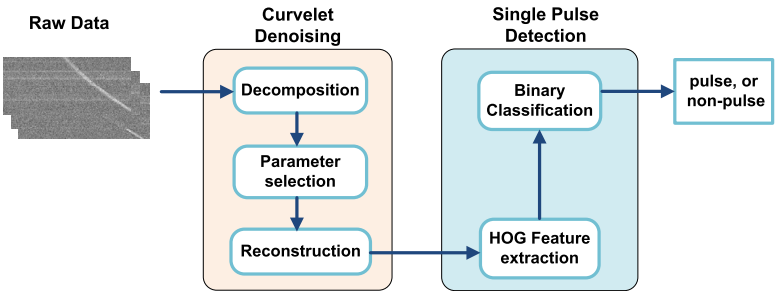

FIGURE 2. The framework of two-stage denoising and detecting method for RRATs time-frequency data. The curvelet denoising approach includes curvelet decomposition, parameters selection and curvelet reconstruction from selective parameters.

Jiang *et al.* [15] presented a wavelet based denoised approach for the de-dispersed time series which is utilized before the single-pulse search. Based on the a priori knowledge of the spin period of RRATs, they applied wavelet reconstruction and shrinkage to the selective frequency bands.

In addition to the above denoising methods used in the astronomical study, image denoising has long been a focus in computer vision. Many filter-based methods have been proposed, for example, block-matching and 3D filtering (BM3D) [16], non-local means filter and its method noise thresholding (NLFMT) [17], and progressive image denoising (PID) [18]. These filter-based methods are efficient in suppressing the noise in slightly corrupted images. There are numerous sparse coding based methods. For example, Xu *et al.* proposed trilateral weighted sparse coding (TWSC) [19] scheme for robust real-world image denoising. Zhang et al. developed group-based sparse representation (GSR) [20] to sparsely represent natural images in the domain of group, which enforces the intrinsic local sparsity and non-local self-similarity of images simultaneously. Lots of supervised learning based methods are proposed for image denoising. Yin *et al.* [21] proposed a model that uses a devised cost function involving semisupervised learning based on a large number of corrupted images with a few labeled training samples. Recently, deep learning based approaches have shown promising results in image denoising and restoration. Dong *et al.* [22] presented a deep learning method for single image super resolution (SR) by an end-to-end mapping between the low/high-resolution images. Mao *et al.* [23] developed a very deep fully convolutional encoding-decoding framework for image restoration which includes symmetrically link convolutional and deconvolutional layers with skip-layer connections. Zhang *et al.* [24] proposed a denoising convolutional neural network (DnCNN) model to handle Gaussian denoising with the unknown noise level. Such deep learning based methods require a large amount of labeled images for training the model.

Different from the above methods, our denoising method is specially designed for the time-frequency RRATs observation data (before de-dispersion) and works for data including weak pulses and the DM values are unknown. The proposed denoising method aims to make curve invisible curve (pulse) visible but not only RFI removal. To the best of our knowledge, there is no existing denoising framework which is specially designed for the time-frequency RRATs data before single pulses detection.

III. CURVELET DENOISING

As shown in Fig. 2, the proposed method has two stages: denoising and detection. In this section, we introduce the denoising method. Considering the dispersion property of radio astronomical signal is shown as a curve in time-frequency plane, and the dispersed curve can be well defined by applying curvelet decomposition together with parameter selection and reconstruction to the time-frequency data, we propose a curvelet based denoising method for radio observation of RRATs. The proposed curvelet denoising approach includes curvelet decomposition, parameters selection and curvelet reconstruction from selective parameters which are presented in Sections III-A and III-B.

A. CURVELET TRANSFORM

Curvelet analysis was first proposed by [27], and then was further implemented on digital data by [28]. It is widely used in image processing, compressed sensing and fluid mechanics, etc [29]. In the two-dimensional (2D) domain $\mathbb{R}^2$, φ_j is considered as a mother cuevelet in the sense that all curvelets at scale 2^{-j} are obtained by rotations and translations of φ_j [30], where the rotation angle $\theta_l = 2\pi \cdot 2^{-\lfloor j/2 \rfloor} \cdot l$, with $l = 0, 1, \ldots,$ such that $0 \leq \theta_l \leq 2\pi$. The translation parameter is $k = (k_1, k_2) \in \mathbb{Z}^2$. With these notations, the curvelets at scale 2^{-j}, orientation θ_l and position $x_k^{j,l} = R_{\theta_l}^{-1}(k_1 \cdot 2^{-j}, k_2 \cdot 2^{-j/2})$ are defined as:

$$\varphi_{j,l,k}(x) = \varphi_j(R_{\theta_l}(x - x_k^{(j,l)})), \tag{1}$$

where R_θ is the rotation by θ radians and R_θ^{-1} is its inverse,

$$R_\theta = \begin{pmatrix} cos\theta & sin\theta \\ -sin\theta & cos\theta \end{pmatrix}. \tag{2}$$

Given a mother curvelet and a set of scales, orientations and positions, the continuous curvelet transform (CCT) of a function $f \in L^2(\mathbb{R}^2)$ is given as:

$$c(j, l, k) = \int_{\mathbb{R}^2} f(x)\overline{\varphi_{j,l,k}(x)}dx, \tag{3}$$

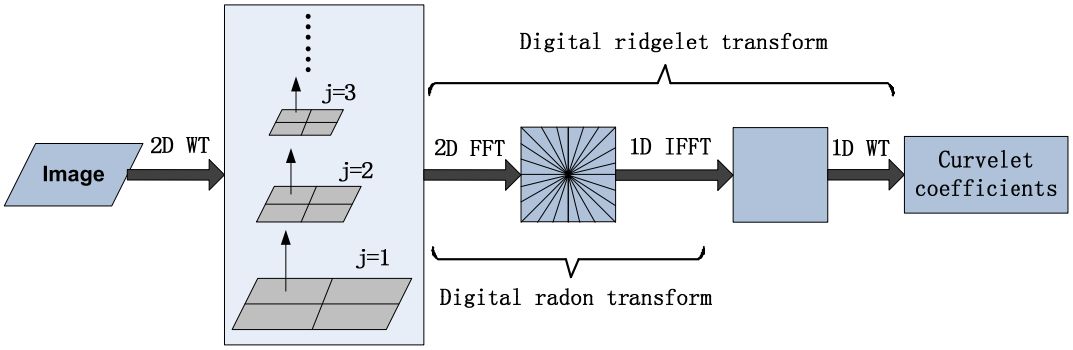

FIGURE 3. The pipeline of digital curvelet transform, where 2D WT stands for the two-dimensional wavelet transform. 2D FFT, 1D IFFT and 1D WT are short for two-dimensional fast fourier transform, one-dimensional inverse fast fourier transform and one-dimensional wavelet transform, respectively.

Because the CCT has three parameters−scale (2^{-j}), rotation angles (θ_l) and translation (k), signal analyzed and synthesized by the CCT yields an output signal controlled by the three parameters.

As shown in Eqn. (3), when taking input as Cartesian arrays of the form $f[t_1, t_2]$, $0 \leq t_1, t_2 \leq n$, the output of digital curvelet transform (DCT) is a collection of coefficients $c^D(j, l, k)$:

$$c^D(j, l, k) = \sum_{0 \leq t_1, t_2 \leq n} f[t_1, t_2] \overline{\varphi^D_{j,l,k}[t_1, t_2]}, \tag{4}$$

Curvelets are based on multiscale ridgelets combined with a spatial bandpass filtering operation to isolate different scales. Fig. 3 shows the pipeline of DCT, which can be summarized as the following two steps: applying 2D WT to the input image, and then applying digital ridgelet transform to the decomposed 2D wavelet sub-bands at different scales.

B. PARAMETER SELECTION

In Eqn. (3), we can see there are three parameters: scale (2^{-j}), rotation angle (θ_l) and translation (k). The scale and the rotation angle represent the width and orientation of the input function $f(x)$, respectively. For a dispersed curve, the curve width depends on the duration of the pulse and the orientation of the curve depends on the DM value of the pulsar, the observation frequency and the bandwidth. Therefore, we select the curvelet parameters (scales and rotation angles) based on the width of the pulse, the DM value of the RRAT, the observation frequency and the bandwidth, and then use the selected parameters for reconstructing the RRAT signal. It should be noted that the exact values of the pulse width and DM are not necessary for the parameter selection step, which justifies the advantage of this DM-free denoising method. We only assume a general range of DM values (10 to 500) and the approximated width of the DM curves to estimate the parameters.

In the following, we will show how to combine the characteristics of dispersed signals and the property of curvelet analysis to derive the equations for parameter selection.

1) SELECTING SCALES

As shown in Fig. 3, 2D WT is used for multi-scale decomposition. The number of scales, N_{scale}, refers to the coarsest wavelet level which can be estimated by:

$$N_{scale} = log_2(min(M, N)) - 3, \tag{5}$$

where $M * N$ is the size of the input image. With the approximated width of the curve in the unit of pixels, we can then estimate the scales that contribute to the description of the curve by:

$$scale\_curve = \lfloor log_2 w \rfloor, \tag{6}$$

where w is the approximated width of the curve in the unit of pixels which is estimated by the full width at half maximum (FWHM) of the pulses. Note that the real width of curve is equal to $w \times t_s$, and t_s is the sampling time which is given in the header information of an observation data.

Now we can estimate the scale levels corresponding to the curve following the rules:

$$\begin{aligned} scale_{min} &= 1, \\ scale_{max} &= \begin{cases} scale\_curve, & \text{if } \mathrm{N_{scale}} \geq \text{scale\_curve}, \\ N_{scale}, & \text{otherwise}. \end{cases} \end{aligned} \tag{7}$$

where $scale_{min}$ is the coarsest scale (level) retained for reconstruction, and $scale_{max}$ is the finest scale (level) retained for reconstruction.

2) SELECTING ORIENTATIONS

At sufficiently fine scales, a curved edge is almost straight. So to capture curved edges, one ought to be able to deploy curvelet in a localized manner, at sufficiently fine scales. The digital curvelet transform uses Radon transform as a component step. As shown in Fig. 4, the Radon transform is a function defined in the space of straight lines L in $\mathbb{R}^2$ by the line integral along each such line. The Radon transform can be expressed as:

$$\begin{aligned} Rtf(\alpha, s) = \int_{-\infty}^{+\infty} f((z \cdot sin\alpha + s \cdot cos\alpha), \\ \times (-z \cdot cos\alpha + s \cdot sin\alpha))dz, \end{aligned} \tag{8}$$

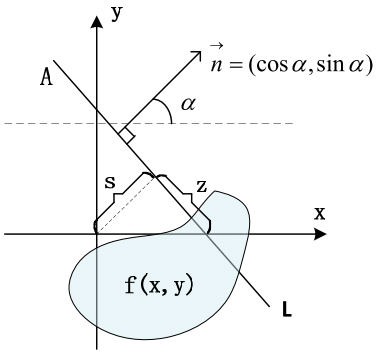

FIGURE 4. Example of Radon transform.

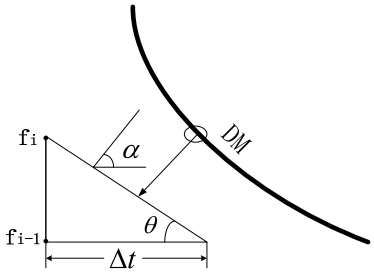

FIGURE 5. Illustration of deriving θ from the DM value.

where α is the orientation parameter θ_l in Eqn. (1). At sufficiently fine scales, a curve can be considered as a straight line. Thus the DM curve in filterbank data (time-frequency data) can be considered as the combination of many straight lines.

The delay time of pulse arrivals between two frequency channels (f_i and f_{i+1}) is estimated by:

$$\Delta t = k_{DM} \cdot (f_{i+1}^{-2} - f_i^{-2}) \cdot DM, \tag{9}$$

where k_{DM} is known as the dispersion constant: $k_{DM} \approx 4.15 \times 10^3 MHz^2 pc^{-1} cm^3 s$. f_{i+1} and f_i are both in MHz (f_i denotes the frequency channel with higher frequency). Fig. 5 shows how to derive θ with DM, here f_{i+1} and f_i are known. Mathematically, it can be calculated by:

$$\theta = arctan \frac{P(f_{i+1} - f_i)}{P(\Delta t)} \tag{10}$$

where $P(\cdot)$ denotes the pixel distance in the image (time-frequency data). $P(f_{i+1} - f_i) = 1$, and $P(\Delta t) = \frac{|\Delta t|}{t_s}$, t_s is the sampling time of the observation data. Then substituting Eqn. (9) into (10), we can find θ:

$$\theta = arctan \left[\frac{t_s}{k_{DM} \cdot \left| f_{i+1}^{-2} - f_i^{-2} \right| \cdot DM} \right]. \tag{11}$$

From Fig. 5, we can obtain $\alpha = 90° - \theta$. Thus, the expression for the curvelet orientation α is further expressed as:

$$\alpha = 90° - arctan \left[\frac{t_s}{k_{DM} \cdot \left| f_{i+1}^{-2} - f_i^{-2} \right| \cdot DM} \right]. \tag{12}$$

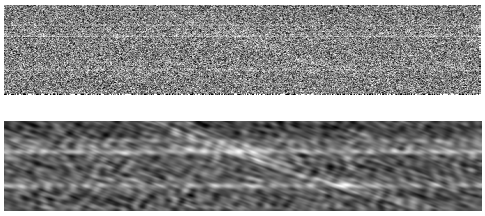

FIGURE 6. The upper panel is a short slice of J1819−1458 time-frequency data which contains a pulse. The lower panel is the corresponding curvelet denoised data. It is reconstructed from scales 1 to 6, and orientations from 22° to 76°. The pulse (curve) is visible in the denoised data.

Algorithm 1 Pseudo Code of Curvelet Denoising

Input: time-frequency data, observation parameters including FWHM, sample time, first frequency channel, number of frequency channel, observation bandwidth
Output: curvelet reconstructed data

```
Apply curvelet decomposition to the data
Calculate scale_min, scale_max according to Eqn. (7)
Initialize α_min = 90, α_max = 0
for i = 1; i <number of frequency channels; i++ do
    Calculate α according to Eqn. (12)
    if α > α_max then
        α_max = α
    else if α < α_min then
        α_min = α
    end if
end for
Reconstruct the data by obtained scale_min, scale_max, α_min, α_max.
```

The main process of curvelet denoising is present in Algorithm 1. In this work, we assume that the typical DM values for RRATs mainly distribute from 10 to 500. The observation frequency and bandwidth can be obtained from the observation data. Then we can estimate the range for α and use this range to reconstruct the time-frequency data. As an example, the sampling time for the observation data of J1819−1458 is 100 μs, frequency of channel 1 (the highest frequency channel) is 1517.75 MHz, bandwidth of one channel is -0.5 MHz, and the number of channels is 512. According to Eqn. (12), α is then calculated to be in the range of 22° to 76°. Fig. 6 shows a short slice of J1819−1458 time-frequency data in which one pulse is detected. The denoised data is reconstructed using scales from 1 to 6, and orientations from 22° to 76°. These selected scales and orientation are expected to contribute to the description of dispersed RRAT signal.

IV. DETECTION METHOD

To evaluate the efficiency of the proposed curvelet-based denoising approach, a method for detecting the single pulses is proposed. The detection approach aims to detect single pulses from the time-frequency data of RRATs. It also treats

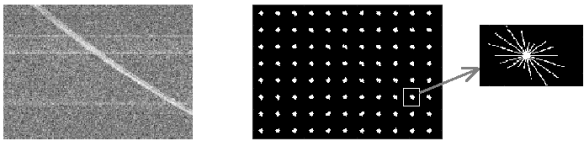

FIGURE 7. The left panel is a slice of J1819−1458 time-frequency data; the middle panel is its computed HOG features; the right panel shows the details of one block in HOG features.

the time-frequency data as images. As shown in Fig. 2, the pulse detection method consists of two steps: feature extraction and classification. The histogram of oriented gradients (HOG) is employed to extract features from images. Then a supervised machine learning method−support vector machine (SVM) is utilized to classify the extracted features into two classes: pulse or non-pulse. The proposed detection method is named as HOG-SVM.

A. FEATURE EXTRACTION

Considering the characteristics of the dispersed curve, we utilize HOG [31], [32] to describe the curve, which uses the gradient (along with horizontal and vertical) information to describe the image (time-frequency data). The magnitude of the gradient is large around edges and corners. The HOG descriptor is invariant to geometric and photometric transformations, except for object orientation. Such changes would only appear in larger spatial regions. Thereby, the advance of HOG is suitable to capture the dispersed curve in astronomical data. Given an image I, its gradient is computed by:

$$\nabla I = \begin{bmatrix} \frac{\partial I}{\partial x} \\ \\ \frac{\partial I}{\partial y} \end{bmatrix}, \tag{13}$$

where $\frac{\partial I}{\partial x}$ and $\frac{\partial I}{\partial y}$ are partial derivatives of the image I in horizontal and vertical directions, respectively. The derivatives of an image can be approximated using finite differences. Then $\frac{\partial I}{\partial x}$ can be calculated by applying a 1D filter to the image I using convolution:

$$\frac{\partial I}{\partial x} = \begin{bmatrix} -1 \\ 1 \end{bmatrix} * I, \tag{14}$$

where $*$ denotes the convolution operation. Fig. 7 shows a short slice of J1819−1458 time-frequency data and the corresponding computed HOG features.

B. CLASSIFICATION

The pulse detection problem is defined as a binary classification task. The class variable assumes one of two values: pulse or non-pulse. Classification is to map the extracted features of the image to the class variable. The training stage is to learn the mapping function. In the classification stage, the learned function is used to predict the class variable using the extracted features. Because of the robustness of the SVM, it has been successfully employed for many applications [33], [34]. We employ the SVM to learn the mapping function. The SVM can do nonlinear classification using kernel functions. Gaussian radial basis function (RBF) kernel is one of the most popular kernels. In this work, the RBF kernel achieves a better performance in classification than other kernels.

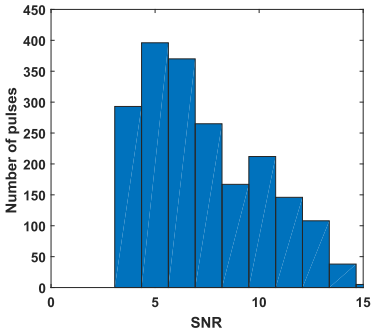

FIGURE 8. SNRs distribution of the generated pulses.

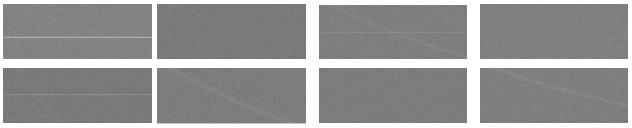

FIGURE 9. Examples of the generated time-frequency data which contain pulses. Some of the generated pulses are invisible caused by their low intensities.

V. EXPERIMENTS AND PERFORMANCE ANALYSIS

This section begins by describing the simulated dataset. Then the performance measurements and experimental settings are presented. Finally, extensive experiments are conducted on the simulated dataset, which evaluate the effectiveness of the proposed denoising and detection methods from several aspects and provide some deep insights into the methods.

A. SIMULATED DATASET

Due to a limited amount of detected RRATs (just over 100) in the wild, the analysis and evaluation of the denoising and detection methods are based on the simulated data. The similar experiments used simulated data for evaluation were conducted in [26] and [35]. The background noise is modeled as white Gaussian noise combined with RFI. The simulated data are displayed in filter bank format, where astrophysical single pulses are dispersed according to Eqn. (9). We assume that the pulse profile is Gaussian with FWHM set between 5 *ms* to 40 *ms*. The observation bandwidth of the simulated data is set to 256 MHz, and the first frequency channel is 1518 MHz. The bandwidth is partitioned into 512 frequency channels, and the sample time is set to 100 μs. The DM value is randomly selected from the integer between 10 to 500. We use the signal-to-noise ratio (SNR) to measure the intensity of the simulated pulses. SNR is calculated from the de-dispersed single-pulse profile and is defined as a ratio of the peak value of the profile to the root mean square of the noise (σ). An emulation set consisting of 22,000 images (each with

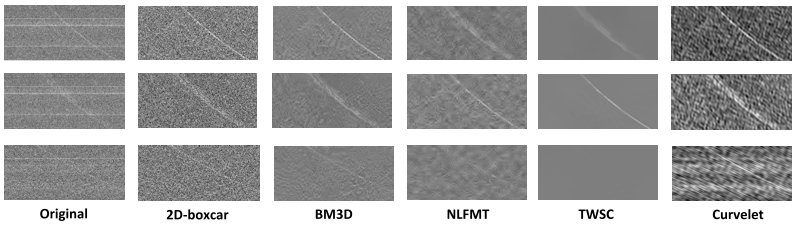

FIGURE 10. Visualized denoising results of three short slices of real RRATs data.

TABLE 1. The detection results based on the data applied with the five denoising methods.

Denosing method	Detection method	FAR(%)	TPR(%)	Accuracy (%)
Original	Blind transform [26]	0	15.2	92.2
BM3D [16]		0	72.1	97.5
2D-boxcar [8]		0	61.5	96.5
TWSC [19]		0	72.0	97.5
NLFMT [17]		0	67.1	97.0
Curvelet (ours)		0	82.7	98.4
Original	HOG-SVM	0.08	15.8	92.3
BM3D [16]		0	80.5	98.2
2D-boxcar [8]		0	64.3	96.8
TWSC [19]		0	81.5	98.3
NLFMT [17]		0	68.5	97.1
Curvelet (ours)		0	**85.5**	**98.7**

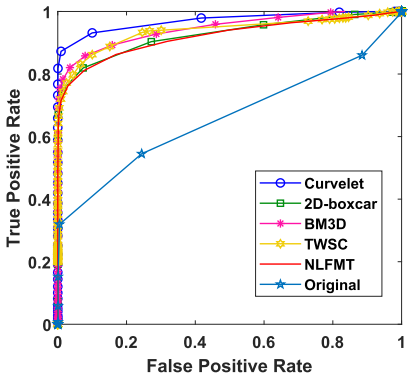

FIGURE 11. Comparison of the blind transform based detection results on original data, 2D-boxcar denoised data, BM3D denoised data, TWSC denoised data, NLFMT denoised data and curvelet denoised data.

TABLE 2. The comparison of computing time taken for denoising.

Denosing method	Time (sec)
BM3D [16]	9.83
2D-boxcar [8]	0.02
TWSC [19]	305.53
NLFMT [17]	235.14
Curvelet	1.08

TABLE 3. The computing time taken for training and testing of the two detection methods.

Detection method	Training (sec)	Testing (sec)
Blind transform [26]	-	68.10
HOG-SVM	253.85	6.17

size 1101 × 512) was generated. Among them, 2,000 images contain a single pulse. The remaining 20,000 images contain no pulse at all. Fig. 8 shows the SNRs distribution of the simulated dataset. One can see most SNRs distribute from 3 to 10. Fig. 9 shows some examples of the generated time-frequency data which contain pulses.

Considering the HOG-SVM detection is a supervised learning method, the dataset is split into the training set and test set. The training set has 17,600 images, among which 1,600 images contain pulses and others do not contain. The testing set has 4,400 images, among which 400 images contain pulses and others do not contain. For a fair comparison, the blind transform based method is evaluated on the test set.

B. PERFORMANCE MEASURES

Three standard terms calculated from the confusion matrix are used to evaluate the final detection results. The three standard terms are:

- *False positive rate (FPR)* is the proportion of negative cases that are incorrectly detected as positive.
- *True positive rate (TPR)* is the proportion of positive cases that are correctly detected.
- *Accuracy* is the proportion of the total number of cases that are correctly detected.

C. EXPERIMENTAL SETTINGS

1) IMPLEMENTATION DETAILS FOR DENOISING

Because there are very limited denoising methods specially designed for RRATs time-frequency data, and most general denoising approaches in image processing can not meet the

TABLE 4. The detection results based on different intensity groups from the five denoising methods.

Denoising method	Detection method	SNR	FAR(%)	TPR(%)	Accuracy (%)
BM3D [16]	Blind transform [26]	SNR $< 5\sigma$	0	29.7	98.4
		$5\sigma \leq$SNR $< 10\sigma$	0	90.1	99.4
		SNR $\geq 10\sigma$	0	100	100
	HOG-SVM	SNR $< 5\sigma$	0	41.8	98.6
		$5\sigma \leq$SNR $< 10\sigma$	0	96.7	99.7
		SNR $\geq 10\sigma$	0	100	100
2D-boxcar [8]	Blind transform [26]	SNRs $< 5\sigma$	0	26.4	98.2
		$5\sigma \leq$SNRs $< 10\sigma$	0	66.2	98.5
		SNRs $\geq 10\sigma$	0	100	100
	HOG-SVM	SNRs $< 5\sigma$	0	32.1	98.4
		$5\sigma \leq$SNRs $< 10\sigma$	0	82.5	99.1
		SNRs $\geq 10\sigma$	0	100	100
TWSC [19]	Blind transform [26]	SNRs $< 5\sigma$	0	31.1	98.5
		$5\sigma \leq$SNRs $< 10\sigma$	0	89.0	99.3
		SNRs $\geq 10\sigma$	0	100	100
	HOG-SVM	SNRs $< 5\sigma$	0	45.1	98.7
		$5\sigma \leq$SNRs $< 10\sigma$	0	97.1	99.7
		SNRs $\geq 10\sigma$	0	100	100
NLFMT [17]	Blind transform [26]	SNRs $< 5\sigma$	0	23.1	98.2
		$5\sigma \leq$SNRs $< 10\sigma$	0	86.2	99.2
		SNRs $\geq 10\sigma$	0	100	100
	HOG-SVM	SNRs $< 5\sigma$	0	35.2	98.5
		$5\sigma \leq$SNRs $< 10\sigma$	0	94.1	99.6
		SNRs $\geq 10\sigma$	0	100	100
Curvelet (ours)	Blind transform [26]	SNR $< 5\sigma$	0	39.6	98.6
		$5\sigma \leq$SNR $< 10\sigma$	0	94.6	99.7
		SNR $\geq 10\sigma$	0	100	100
	HOG-SVM	SNR $< 5\sigma$	0	47.3	98.8
		$5\sigma \leq$SNR $< 10\sigma$	0	98.7	99.9
		SNR $\geq 10\sigma$	0	100	100

requirement for denoising RRATs data, we compare the proposed denoising method with four methods. The first one is a traditional denoising method used in radio astronomy−2D-boxcar method. It is similar to the boxcar smoothing [8] which smooths the time-frequency data along both time-axis and frequency-axis. The second is a filter based denoising method: BM3D [16]. The third is another filtered based method: NLFMT [17]. The last one is a sparse coding based method: TWSC [19]. The size of the input image is 1101×512. For parameter setting of 2D-boxcar, the width of the boxcar is set to 10 along both axes. For BM3D, the standard deviation of the noise is set to 10, the profile is set to 'normal profile'. For NLFMT, the neighbor window size is set to 7, the search window size is 21, σ for Gaussian kernel generation is 5, the wavelet transform level is 3, 'db8' is selected as a mother wavelet, and thresholding type is soft. For TWSC, the patch size is set to 6, the step of two neighbor patches is 3, and the size of the window around the patch is 20.

2) IMPLEMENTATION DETAILS FOR DETECTION

To evaluate the proposed HOG-SVM detection method, we compare it to the blind transform based detection approach [26]. Considering the size of 2D-boxcar denoised images are smaller than the other four methods denoised images, we apply different HOG parameters to the data. For 2D-boxcar denoised data, the number of bins is set to 9, the number of horizontal cells is 13, the number of vertical cells is 6, the cell size is 8×8. For BM3D, TWSC, NLFMT and curvelet denoised data, the number of bins is set to 9, the number of horizontal cells is 36, the number of vertical cells is 17, the cell size is 30×30. The SVM model is trained with the RBF kernel.

D. EXPERIMENTAL RESULTS

1) COMPARISONS BETWEEN THE DIFFERENT DENOISING AND DETECTION METHODS

In this part, we conduct an experiment to evaluate the performance of the five denoising methods. Fig. 10 shows the visual denoising results of 2D-boxcar, BM3D, TWSC, NLFMT and curvelet denoising method. It can be seen that the dispersed curves are well reconstructed by the curvelet denoising method. Fig. 11 shows the detection results obtained by the blind transform based method from the original data, 2D-boxcar denoised data, BM3D denoised data, TWSC denoised data, NLFMT denoised data and curvelet denoised data. The plotting is the receiver operating characteristic (ROC) curve which illustrates the diagnostic ability of a detection system as its discrimination threshold is varied. Among the five sets of denoised data, BM3D and TWSC have similar performance. The best performance is achieved on curvelet denoised data. This indicates that the proposed curvelet based denoising method is superior to the other four denoising methods.

Table 1 shows the detection results based on the five denoising methods using two detection methods. First, one can see that both detection methods achieve better results on

TABLE 5. The detection results based on different DM groups from the five denoising methods.

Denoising method	Detection method	SNR	FAR(%)	TPR(%)	Accuracy (%)
BM3D [16]	Blind transform [26]	$10 \leq$DMs < 200	0	79.7	99.1
		$200 \leq$DMs < 350	0	71.6	99.0
		$350 \leq$DMs ≤ 500	0	63.4	99.2
	HOG-SVM	$10 \leq$DMs < 200	0	69.7	98.7
		$200 \leq$DMs < 350	0	84.9	99.4
		$350 \leq$DMs ≤ 500	0	86.4	99.6
2D-boxcar [8]	Blind transform [26]	$10 \leq$DMs < 200	0	68.5	98.8
		$200 \leq$DMs < 350	0	60.9	98.6
		$350 \leq$DMs ≤ 500	0	48.9	98.9
	HOG-SVM	$10 \leq$DMs < 200	0	36.8	97.4
		$200 \leq$DMs < 350	0	70.5	98.9
		$350 \leq$DMs ≤ 500	0	81.8	99.6
TWSC [19]	Blind transform [26]	$10 \leq$DMs < 200	0	79.5	99.2
		$200 \leq$DMs < 350	0	70.1	98.9
		$350 \leq$DMs ≤ 500	0	68.2	99.3
	HOG-SVM	$10 \leq$DMs < 200	0	80.9	99.2
		$200 \leq$DMs < 350	0	82.9	99.3
		$350 \leq$DMs ≤ 500	0	86.4	99.6
NLFMT [17]	Blind transform [26]	$10 \leq$DMs < 200	0	71.1	98.9
		$200 \leq$DMs < 350	0	65.8	98.8
		$350 \leq$DMs ≤ 500	0	63.6	99.2
	HOG-SVM	$10 \leq$DMs < 200	0	83.1	99.3
		$200 \leq$DMs < 350	0	80.1	99.3
		$350 \leq$DMs ≤ 500	0	83.0	99.6
Curvelet (ours)	Blind transform [26]	$10 \leq$DMs < 200	0	90.9	99.6
		$200 \leq$DMs < 350	0	80.8	99.3
		$350 \leq$DMs ≤ 500	0	70.4	99.4
	HOG-SVM	$10 \leq$DMs < 200	0	86.8	99.5
		$200 \leq$DMs < 350	0	80.1	99.3
		$350 \leq$DMs ≤ 500	0	92.6	99.8

curvelet denoised data than the other four data. Applying the curvelet based denoising method to RRATs time-frequency data leads to better pulse detection results. This further justifies the advantage of applying the proposed curvelet based denoising method. Second, the HOG-SVM method achieves higher TPR than the blind transform method on the five sets of denoised data. This significant improvement in detection accuracy shows that the effectiveness of the proposed HOG-SVM single pulse detection method. Finally, we can see the combination of curvelet denoising and HOG-SVM single pulse detection leads to the best performance with TPR 85.5% and accuracy 98.7% on the simulated dataset.

We also report the comparison of computing time taken for denoising and detection. All of the methods are implemented by Matlab code. On our computer with i7-3770 CPU and 16.0-G memory, the computing time of denoising and detection are given in Tables 2 and 3, respectively. The denoising time is the average time cost for each image. From Table 2 one can see that our method takes significantly less time than BM3D, TWSC and NLFMT. The HOG-SVM method contains training and testing phases, while the blind transform does not contain a training phase. Table 3 shows the average time taken for training and testing of the two detection methods on the five sets of denoised data.

2) THE EFFICIENCY ON DIFFERENT INTENSITY GROUPS

To further justify the efficiency of the proposed method, we conduct an experiment by dividing the test set of simulated data into three groups based on the intensity of the single pulse. The data (simulated pulses) are grouped by their SNRs: weak pulses (SNR $< 5\sigma$), medium pulses ($5\sigma \leq$SNR $< 10\sigma$) and strong pulses (SNR $\geq 10\sigma$). The HOG-SVM classification model is learned from the training set and separated tested on each intensity group. Here each intensity group consists of the images that contain the pulses with specific intensities and 4000 images do not contain pulses.

Table 4 shows the detection results based on the three intensity groups from the BM3D denoised data and 2D-boxcar denoised data, TWSC denoised data, NFLMT denoised data and curvelet denoised data. Note that SNRs are computed from the de-dispersed simulated data. The detection results from the curvelet denoised data are better than the other four sets of data, this again demonstrates the effectiveness of the proposed denoising method. More importantly, one can see that both detection methods achieve the best performance on the strong pulses group (with TPR 100%), and their performances significantly drop on weak pulses group. This indicates that it is more challenge to detect the weak intensity of pulses.

Though both detection methods achieve lower detection rates on weak pulses, the HOG-SVM shows more robust on weak pulses detection than the blind transform based method. Considering there is a large amount of weak radio astronomical observation in the wild, the HOG-SVM is effective for single pulse detection.

TABLE 6. The comparison of detection results using different classification methods.

Method	FAR(%)	TPR(%)	Accuracy (%)	Training (sec)	Testing (sec)
SVM	0	85.5	98.7	268.2	9.7
Logic regression	1.7	80.8	96.7	2204.4	1.0
KNN	0	74.7	97.7	517.8	57.9

3) THE EFFICIENCY ON DIFFERENT DM GROUPS

We also analyze the efficiency of the proposed denoising and detection methods from the aspect of the influence brought by various DM values. The pulses in the test set are divided into three groups by their DM values: $10 \leq$DM < 200, $200 \leq$DM < 350 and $350 \leq$DM ≤ 500. The HOG-SVM classification model is learned from the training set and tested separately on each DM group. Here each DM group consists of the images contain the pulses with specific DMs and 4000 images do not contain pulses.

Table 5 shows the detection results based on the three DM groups from the five sets of denoised data, respectively. It is interesting to see that the two detection methods achieve the best performance in different DM groups. The HOG-SVM shows more effective for the pulses with relatively large DM values, while the blind transform based method is more effective for the pulses with relatively small DM values. In addition, from Table 5, one can see that the overall detection results from curvelet denoised data are better than the other four sets of denoised data.

4) PERFORMANCE OF DIFFERENT CLASSIFICATION METHODS

We discuss the influence of different classification methods on detection. Considering the robustness of the SVM, we employ the SVM to learn the mapping function in this work. To analyze the influence of different classification methods, we conduct an experiment to compare the performance of SVM with the other two methods. One is logic regression classifier, another is k-nearest neighbors algorithm (KNN). In this experiment, all the methods use the HOG features extracted from the curvelet denoised data. The results with various measures are shown in Table 6. One can see that the SVM outperforms the other two methods. We also show the computing time taken for training and testing. The SVM takes significantly less time for training than the other two methods.

VI. CONCLUSION

It is desirable to conduct single pulse detection on RRATs time-frequency data before applying de-dispersion. Considering the strong background noise existing in the data, we propose a curvelet-based denoising approach for time-frequency data of RRATs. Taking into account the characteristics of the RRAT pulses and the noise, the denoising approach estimates the range of curvature (orientations) and width (scales) contributing to the description of an RRATs pulse and reconstructs the data from the selected orientations and scales. The proposed denoising approach does not require the prior knowledge of an exact DM value for processing the data. Moreover, to justify the curvelet based denoising approach and address the RRAT single pulse detection problem, a single detection method HOG-SVM is developed. All experiments are conducted on a simulated dataset. The experimental results show that applying curvelet based denoising to RRATs data leads to significantly higher pulse detection accuracy compared with the BM3D, 2D-boxcar, TWSC and NLFMT denoising methods. The HOG-SVM method achieves higher detection accuracy than the blind transform based detection method on the test set. Furthermore, we analyze the denoising and detection methods by evaluating their performance on different pulse intensities and DM values. The HOG-SVM method shows more robust on weak pulses and pulses with relatively larger DM values. For future work, we will extend the proposed denoising and detection approach to other dispersed astronomical signal detection.

ACKNOWLDGMENT

We would like to thank the Parkes radio telescope which provided the RRATs observation data in this work.

REFERENCES

[1] M. A. McLaughlin, A. G. Lyne, D. R. Lorimer, M. Kramer, A. J. Faulkner, R. N. Manchester, J. M. Cordes, F. Camilo, A. Possenti, I. H. Stairs, G. Hobbs, N. D'Amico, M. Burgay, and J. T. O'Brien, "Transient radio bursts from rotating neutron stars," *Nature*, vol. 439, pp. 817–820, Feb. 2006.

[2] S. Larsson, "Parameter estimation in epoch folding analysis," *Astron. Astrophys. Suppl.*, vol. 117, pp. 197–201, May 1996.

[3] N. Roberts, D. Lorimer, and M. Kramer, *Handbook of Pulsar Astronomy*. Cambridge, U.K.: Cambridge Univ. Press, 2005, pp. 127–143.

[4] W. Zhao, Y. Lv, Q. Liu, and B. Qin, "Detail-preserving image denoising via adaptive clustering and progressive PCA thresholding," *IEEE Access*, vol. 6, no. 1, pp. 6303–6315, 2018.

[5] J. Yu, L. Tan, S. Zhou, L. Wang, and M. A. Siddique, "Image denoising algorithm based on entropy and adaptive fractional order calculus operator," *IEEE Access*, vol. 5, no. 6, pp. 12275–12285, 2017.

[6] L. Sun, B. Jeon, Y. Zheng, and Z. Wu, "A novel weighted cross total variation method for hyperspectral image mixed denoising," *IEEE Access*, vol. 5, pp. 27172–27188, Nov. 2017.

[7] J.-L. Starck, E. J. Candes, and D. L. Donoho, "The curvelet transform for image denoising," *IEEE Trans. Electron. Packag. Manuf.*, vol. 11, no. 6, pp. 670–684, Jun. 2002.

[8] J. M. Cordes and M. A. McLaughlin, "Searches for fast radio transients," *Astrophys. J.*, vol. 596, pp. 1142–1154, Oct. 2003.

[9] J. S. Deneva *et al.*, "Arecibo pulsar survey using ALFA: Probing radio pulsar intermittency and transients," *Astrophys. J.*, vol. 703, pp. 2259–2274, Sep. 2009.

[10] E. F. Keane, D. A. Ludovici, R. P. Eatough, M. Kramer, A. G. Lyne, M. A. McLaughlin, and B. W. Stappers, "Further searches for rotating radio transients in the parkes multi-beam pulsar survey," *Monthly Notices Roy. Astronomical Soc.*, vol. 401, pp. 1057–1068, Jan. 2010.

[11] M. Bagchi, A. C. Nieves, and M. McLaughlin, "A search for dispersed radio bursts in archival parkes multibeam pulsar survey data," *Monthly Notices Roy. Astronomical Soc.*, vol. 425, pp. 2501–2506, Oct. 2012.

[12] B.-Y. Cui, J. Boyles, M. A. McLaughlin, and N. Palliyaguru, "Timing solution and single-pulse properties for eight rotating radio transients," *Astrophys. J.*, vol. 840, no. 1, p. 5, Apr. 2017.

[13] A. B. Romeo, C. Horellou, and J. Bergh, "A wavelet add-on code for new-generation N-body simulations and data de-noising (JOFILUREN)," *Monthly Notices Roy. Astronomical Soc.*, vol. 354, no. 4, pp. 1208–1222, Nov. 2004.

[14] R. P. Eatough, E. F. Keane, and A. G. Lyne, "An interference removal technique for radio pulsar searches," *Monthly Notices Roy. Astronomical Soc.*, vol. 395, no. 1, pp. 410–415, Apr. 2009.

[15] M. Jiang, B.-Y. Cui, N. A. Schmid, M. A. McLaughlin, and Z.-C. Cao, "Wavelet denoising of radio observations of rotating radio transients (RRATs): Improved timing parameters for eight RRATs," *Astrophys. J.*, vol. 847, no. 1, p. 75, Sep. 2017.

[16] K. Dabov, A. Foi, V. Katkovnik, and K. Egiazarian, "Image denoising with block-matching and 3D filtering," *Proc. SPIE*, vol. 6064, Feb. 2006, Art. no. 606414.

[17] B. K. S. Kumar, "Image denoising based on non-local means filter and its method noise thresholding," *Signal, Image Video Process.*, vol. 7, no. 6, pp. 1211–1227, 2013.

[18] C. Knaus and M. Zwicker, "Progressive image denoising," *IEEE Trans. Image Process.*, vol. 23, no. 7, pp. 3114–3125, Jul. 2014.

[19] J. Xu, L. Zhang, and D. Zhang, "A trilateral weighted sparse coding scheme for real-world image denoising," in *Proc. Eur. Conf. Comput. Vis.*, Sep. 2018, pp. 20–36.

[20] J. Zhang, D. Zhao, and W. Gao, "Group-based sparse representation for image restoration," *IEEE Trans. Image Process.*, vol. 23, no. 8, pp. 3336–3351, Aug. 2014.

[21] J.-L. Yin, B.-H. Chen, and Y. Li, "Highly accurate image reconstruction for multimodal noise suppression using semisupervised learning on big data," *IEEE Trans. Multimedia*, vol. 20, no. 11, pp. 3045–3056, Nov. 2018.

[22] C. Dong, C. C. Loy, K. He, and X. Tang, "Learning a deep convolutional network for image super-resolution," in *Proc. Eur. Conf. Comput. Vis.*, 2014, pp. 184–199.

[23] X. Mao, C. Shen, and Y.-B. Yang, "Image restoration using very deep convolutional encoder-decoder networks with symmetric skip connections," in *Proc. Adv. Neural Inf. Process. Syst.*, 2016, pp. 2802–2810.

[24] K. Zhang, W. Zuo, Y. Chen, D. Meng, and L. Zhang, "Beyond a Gaussian denoiser: Residual learning of deep CNN for image denoising," *IEEE Trans. Image Process.*, vol. 26, no. 7, pp. 3142–3155, Jul. 2017.

[25] B. Zackay and E. O. Ofek, "An accurate and efficient algorithm for detection of radio bursts with an unknown dispersion measure, for single dish telescopes and interferometers," *Astrophys. J.*, vol. 835, no. 1, p. 11, Jan. 2017.

[26] M. Alkhweldi, N. A. Schmid, and R. M. Prestage, "A blind transform based approach for the detection of isolated astrophysical pulses," in *Proc. IEEE Int. Conf. Acoust., Speech Signal Process. (ICASSP)*, New Orleans, LA, USA, Mar. 2017, pp. 3944–3948.

[27] E. J. Candes and D. L. Donoho, "Curvelets: A surprisingly effective nonadaptive representation for objects with edges," in *Proc. 4th Int. Conf. Curves Surf.*, Saint-Malo, France, vol. 2, Jul. 1999.

[28] D. L. Donoho and M. R. Duncan, "Digital curvelet transform: Strategy, implementation, and experiments," *Proc. SPIE*, vol. 4056, pp. 12–31, Apr. 2000.

[29] Y. Yang, S. Tong, S. Huang, P. Lin, and Y. Fang, "A hybrid method for multi-focus image fusion based on fast discrete curvelet transform," *IEEE Access*, vol. 5, pp. 14898–14913, 2017.

[30] E. Candès, L. Demanet, D. Donoho, and X. Ying, "Fast discrete curvelet transforms," *Multiscale Model. Simul.*, vol. 5, no. 3, pp. 861–899, Sep. 2006.

[31] N. Dalal and B. Triggs, "Histograms of oriented gradients for human detection," in *Proc. IEEE Comput. Soc. Conf. Comput. Vis. Pattern Recognit.*, vol. 1, Jun. 2005, pp. 886–893.

[32] Z. Xiang, H. Tan, and W. Ye, "The excellent properties of a dense grid-based HOG feature on face recognition compared to Gabor and LBP," *IEEE Access*, vol. 6, pp. 29306–29319, Mar. 2018.

[33] G. Guo, S. Z. Li, and K. L. Chan, "Support vector machines for face recognition," *Image Vis. Comput.*, vol. 19, nos. 9–10, pp. 631–638, 2001.

[34] A. Statnikov, D. Hardin, and C. Aliferis, "Using SVM weight-based methods to identify causally relevant and non-causally relevant variables," *Sign*, vol. 1, p. 4, 2006.

[35] K. Dabov, A. Foi, V. Katkovnik, and K. Egiazarian, "An accurate and efficient algorithm for detection of radio bursts with an unknown dispersion measure, for single-dish telescopes and interferometers," *IEEE Trans. Image Process.*, vol. 16, no. 8, pp. 2080–2095, Aug. 2007.

MIN JIANG received the B.S. and M.S. degrees in electrical engineering from the China University of Mining and Technology, Beijing, China. She is currently pursuing the Ph.D. degree with the Lane Department of Computer Science and Electrical Engineering, West Virginia University. She is also a Visiting Scholar with the Department of Statistics and the Institute of Intelligent Finance, Accounting and Taxation, Guangzhou University. Her research interests include computer vision, machine learning, and signal processing, in particular, astronomical signal denoising, and BMI analysis from human visual appearance.

BINGYI CUI received the B.S. degree in physics from Nanjing University, Nanjing China. He is currently pursuing the Ph.D. degree with the Department of Physics, West Virginia University. His research interests include radio astronomy, astrophysics, and theoretical astrophysics.

YU-FENG YU received the Ph.D. degree in statistics from Sun Yat-sen University, Guangzhou, China. From 2016 to 2017, he was a Visiting Scholar with the Lane Department of Computer Science and Electrical Engineering, West Virginia University, Morgantown, WV, USA. From 2017 to 2018, he was a Senior Research Associate with the Department of Electronic Engineering, City University of Hong Kong. He is currently an Assistant Professor with the Department of Statistics, Guangzhou University. His research interests include image processing, statistical optimization, pattern recognition, and machine learning.

ZHICHENG CAO received the B.S. and M.S. degrees in biomedical engineering from Xi'an Jiaotong University, China, and the Ph.D. degree in electrical engineering from West Virginia University. He is currently an Assistant Professor with the Biomedical Engineering Department, Xidian University, China. He has authored nearly 20 papers. His research interests include biometrics, pattern recognition, and machine learning with a focus on multi- and cross-spectral face/periocular recognition and heterogeneous image quality. He is a member of SPIE.